Volume 28
Number 14
14 April 2026
Pages 2085–2276

CrystEngComm

rsc.li/crystengcomm

ISSN 1466-8033

ROYAL SOCIETY OF CHEMISTRY

PAPER
Faiza Mokhtari *et al.*
Bubble behavior in titanium doped sapphire crystals: from micro to macro scale

CrystEngComm

ROYAL SOCIETY OF CHEMISTRY

PAPER

View Article Online
View Journal | View Issue

Cite this: *CrystEngComm*, 2026, **28**, 2125

Bubble behavior in titanium doped sapphire crystals: from micro to macro scale

Nicolas Pruneau,[ab] Faiza Mokhtari, *[a] Abdeldjelil Nehari,[a] Romain Jandot,[ac] Ahmed Nouri,[b] Omar Boucheikha[b] and Kheirreddine Lebbou [a]

This work presents a comprehensive experimental and numerical investigation of bubble formation, motion, and entrapment in titanium-doped sapphire (Ti:Al_2O_3) crystals from micro to large-scale. Crystals of 5 mm, 30 mm, and 260 mm diameters were grown using distinct furnace configurations, enabling systematic comparison of bubble morphology and density across crystal scale. In all cases, the seed orientation was (11–20) and the average titanium concentration was around 300 ppm. A global finite element model was developed to simulate coupled heat and mass transfer in the growth systems, including heat conduction, buoyant and thermocapillary (Marangoni) convection, internal and surface radiation, and forced convection induced by pulling or rotation. In μ-PD sapphire rods ($D \approx 5$ mm), the strong thermal gradients (270–680 K cm^{-1}), forced convection induced by rod pulling and Marangoni convection close to the meniscus, promote bubble accumulation and entrapment. Optical microscopy revealed bubbles ranging from 10 to 70 μm, with different morphology and size evolving with the pulling rate and Ti concentration. In contrast, Cz-grown crystals ($D \approx 30$ mm) exhibited lower temperature gradients (150–300 K cm^{-1}) and efficient bubble removal due to enhanced upward flow near the crucible sidewall and large free surface area, resulting in a nearly bubble-free central zone. For large-diameter crystals ($D \approx 260$ mm), the highly convex interface and small upward buoyant flow with a small free surface area (compared to the crucible cross section) limit gas evacuation, leading to localized peripheral bubble zones. The strong correlation between simulations and experiments demonstrates that bubble dynamics in Ti:sapphire growth are governed by the interaction of Marangoni, buoyant, and forced convection and titanium concentration. These insights provide key guidelines for optimizing furnace design and growth parameters to minimize gas inclusions and improve optical quality in high-performance laser crystals.

Received 25th December 2025,
Accepted 3rd March 2026

DOI: 10.1039/d5ce01214g

rsc.li/crystengcomm

1. Introduction

Titanium-doped sapphire (Ti:α-Al_2O_3, or Ti:sapphire) is a cornerstone material in advanced optical technologies, forming the basis of femtosecond and petawatt-class laser systems. Its exceptionally broad tunable emission range (650–1100 nm), high optical transparency across the visible and near-infrared regions, and outstanding thermo-mechanical stability make it ideally suited for high-performance laser applications.[1–17] Since its development in the 1980s at MIT Lincoln Laboratory,[2] Ti:sapphire has driven continuous innovation in ultrafast laser technology. Current research efforts primarily focus on optimizing crystal growth methods to produce large, defect-free crystals exhibiting high optical homogeneity and uniform dopant distribution.

A major challenge in Ti:sapphire crystal growth is the formation of inclusions – mostly gas filled bubbles, which arise from multiple physicochemical processes during solidification. Bubble formation can result from the chemical composition of the growth atmosphere, influenced by the inert gas used and the materials constituting the thermal environment. Both factors determine the atmosphere's chemical potential and its oxidizing or reducing nature, directly affecting growth mechanisms.[18,19] Additional contributing factors include the release of dissolved gases during raw material melting,[20] thermal dissociation of alumina,[21,22] chemical reactions between the melt and crucible materials such as molybdenum, tungsten, or iridium,[23] and the local titanium dopant concentration.[24] Bubbles can nucleate at the solid–liquid interface or become entrained within convective melt flows, eventually being trapped within the growing crystal lattice.

[a] *Institut Lumière Matière, UMR5306 CNRS, Université de Lyon 1, 69622 Villeurbanne, Cedex, France. E-mail: faiza.mokhtari@univ-lyon1.fr*
[b] *ECMGreentech/Cyberstar Rue de Chamrousse, Voie des Collines, 38800 Le Pont-de-Claix, France*
[c] *Amplitude Group, 2 rue du Bois Chaland, 91090 Lisses, France*

The presence of such inclusions significantly degrades optical performance by inducing light scattering and localized heating, which promote mechanical stress, crack initiation, and reduced laser efficiency. Large inclusions (>100 μm) exacerbate these effects through enhanced absorption and local thermal gradients, increasing the likelihood of crystal fracture.[9,10] The density and spatial distribution of bubbles are strongly governed by melt convection, temperature gradients, and the morphology of the solidification front. Consequently, precise control over growth parameters such as the pulling rate, temperature distribution, and crucible geometry is essential to suppress bubble entrapment and ensure the production of high-quality Ti:sapphire crystals.

Pioneering studies by K. Lebbou's team at the Institut Lumière Matière (ILM), France, have provided significant insights into defect formation mechanisms, including bubble and crack dynamics, during Ti:sapphire crystal growth using melt-based techniques such as micro-pulling-down (μ-PD) and the Czochralski (CZ) method. In μ-PD growth, the pulling rate exerts a dominant influence on crystal quality: slower growth rates (<1 mm min^{-1}) effectively minimize bubble incorporation, yielding superior crystal homogeneity.[25–27] When bubbles approach the solid–liquid interface, they exhibit periodic oscillations, alternately entering and leaving the interface. After several cycles, increasing oscillation amplitude leads to bubble entrapment.[28] Analytical and experimental studies of titanium segregation during μ-PD growth further revealed that high pulling rates (5–16.7 μm s^{-1}) produce stationary dopant distributions, whereas lower rates (~0.2 μm s^{-1}) induce Gulliver–Scheil-type segregation.[29]

Investigations of bubbles in Czochralski-grown sapphire are more limited. In undoped sapphire, bubbles tend to be smaller (2–5 μm) and more spherical compared to those in Ti:sapphire crystals (10–45 μm). Both bubble density and size increase with pulling and rotation rates, with the pulling rate exerting the stronger influence.[24,30,31] For the Kyropoulos (Ky) method, research led by Lebbou's team has primarily focused on titanium segregation phenomena and the so-called "milky defect".[32–35]

Beyond experimental efforts, several computational studies have provided complementary insight into melt convection, heat transfer, and interface dynamics in sapphire growth across different methods, including μ-PD, CZ, and Kyropoulos. Numerical modeling of sapphire crystal growth has advanced substantially for both the Czochralski (CZ) and Kyropoulos (KY) techniques, which together dominate industrial production of high-purity single-crystal Al_2O_3. Both methods operate in a strongly coupled multiphysics environment involving buoyancy- and Marangoni-driven turbulent melt convection, radiative heat transfer in semitransparent media, and steep thermal gradients that generate substantial thermoelastic stresses and growth defects.

In the Czochralski process, the crystal is rotated and pulled from the melt, and numerical studies focused on global models of heat and mass transfer.[36–41] These advances have enabled quantitative prediction of interface morphology and large-diameter stress distributions. In contrast, the Kyropoulos technique maintains the crystal largely immersed in the melt, with growth governed by radiative balance and controlled cooling.[42–47]

Particularly, the effects of additional resistive bottom heating and crystal rotation have been studied for Kyropoulos sapphire crystal growth, examined under various crucible geometries.[46,47] Their results demonstrated that crucibles with curved or sloped corners, combined with bottom heating, substantially reduced the melt–crystal interface convexity (by up to 48%) and suppressed convective flow intensity compared with cylindrical crucibles.

Numerical studies of the micro-pulling-down (μ-PD) method remain comparatively limited. Early work by Lan *et al.*[48] established the foundation by modeling convection-driven solute transport in Ge–Si melts. This was extended[49–51] to introduce parametric, dynamic, and global-scale simulations of sapphire fiber growth, revealing key thermal-capillary effects and furnace-wide temperature distributions. More recent efforts have focused on dopant segregation[52,53] and interfacial phenomena such as dewetting,[54] progressively advancing toward global multiphysics models. Although these studies demonstrate the growing predictive power of numerical modeling for crystal quality and process optimization, most still rely on simplifying assumptions that limit accurate representation of complex experimental growth dynamics.

Recently, we developed and validated a global finite element model to investigate bubble behavior in undoped sapphire rods grown by the μ-PD technique.[55] The results elucidate the critical role of meniscus geometry and convective mechanisms in governing bubble incorporation. When the crystal diameter closely matches the die capillary diameter, the meniscus adopts a nearly cylindrical shape with minimal height and radial curvature, reducing both Marangoni convection at the periphery and forced convection in the core. This configuration enables complete suppression of bubbles at low pulling rates (*e.g.*, 0.25 mm min^{-1}), as evidenced by the absence of peripheral bubble rings and core voids in experimental observations.

By integrating experimental characterization with Multiphysics finite element simulations, this study aims to elucidate the mechanisms governing bubble formation, distribution, and evolution in Ti:sapphire crystals across different growth scales. Crystals of 5 mm, 30 mm, and 260 mm diameters were grown by Lebbou's team at ILM Institute (France) using distinct furnace configurations (Fig. 1). The combination of micro- to macro-scale analysis enables a comprehensive understanding of the interaction between temperature fields, flow dynamics, and interface morphology, which are key factors determining crystal quality and optical performance.

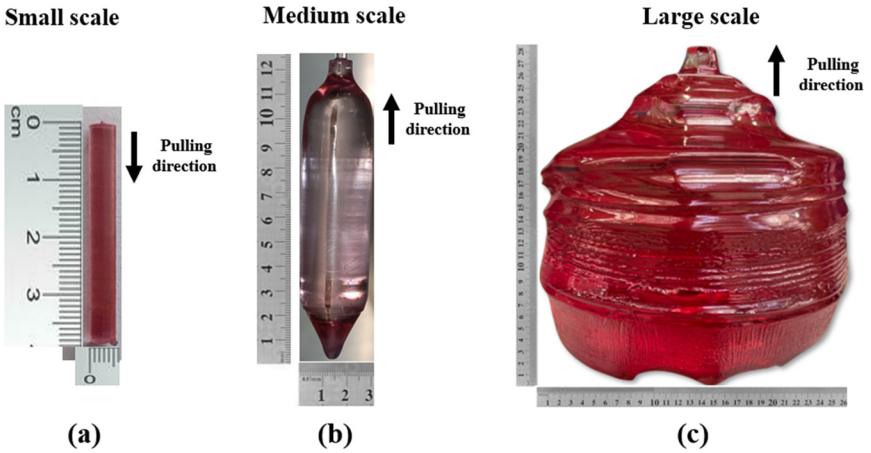

Fig. 1 Titanium-doped sapphire crystals grown by K. Lebbou's group at the ILM Laboratory, illustrating growth from small and medium scales to large scale. (a) μ-PD rod with D = 5 mm and L = 38 mm; (b) CZ-grown boule with D = 30 mm and L = 125 mm; (c) large crystal D = 258 mm and L = 276 mm.

2. μ-PD growth of Ti-doped sapphire rods ($D \sim 5$ mm)

A high-quality titanium-doped sapphire (Al_2O_3:Ti^{3+}) single crystal was successfully grown using the micro-pulling-down (μ-PD) method. The obtained rod-shaped crystal, shown in Fig. 1(a), measured 38 mm in length, had an almost uniform 5 mm diameter, weighed 2.8 g, and exhibited a transparent light-red coloration typical of Ti^{3+} ions incorporated into the corundum lattice.

The growth was carried out in a radio-frequency induction-heated μ-PD furnace (Fig. 2a). The crucible (outer diameter 22 mm, inner diameter 20 mm, height 49 mm) with a capillary die at its bottom (die diameter 5 mm, orifice diameter 1 mm; Fig. 2) was used. An after-heater (height 50 mm, outer/inner diameter 22/20 mm) surrounded the lower part of the crucible and extended the high-temperature zone downward, significantly reducing the axial thermal gradient at the solidification interface and minimizing thermal stress in the growing crystal. The entire assembly was surrounded by insulation and enclosed within a transparent quartz tube, which provided thermal stability, chemical inertness, and excellent optical access for real-time monitoring of the crystal during growth. A narrow observation channel was drilled through the after-heater and insulation (Fig. 2b) to allow direct visual control of the growth zone beneath the crucible; the channel diameter was minimized to limit the disturbance of radial temperature symmetry.

The charge consisted of 5.2 g of high-purity raw materials: undoped Al_2O_3 crackle, undoped and Ti-doped Al_2O_3 micro-beads. Before heating, the chamber was evacuated to approximately 10^{-4} mbar and then filled with flowing high-purity argon to prevent oxidation of the crucible and after-heater. Two preliminary melting cycles were performed to establish a stable pendant drop at the die orifice. Seeding was accomplished using the undoped sapphire seed crystal at a constant pulling rate of 0.5 mm min^{-1}.

Because of the extremely steep temperature gradient inherent to the μ-PD technique, the seed was moved very slowly to the molten drop to avoid thermal shock. Contact was followed by slight partial melting of the seed tip to form a stable meniscus. The height (h_m) and shape of the meniscus, governed by surface tension, growth angle, and the precise vertical position of the solid–liquid interface relative to the die, were carefully adjusted throughout the process. Stable meniscus control proved essential for maintaining constant crystal diameter and achieving high

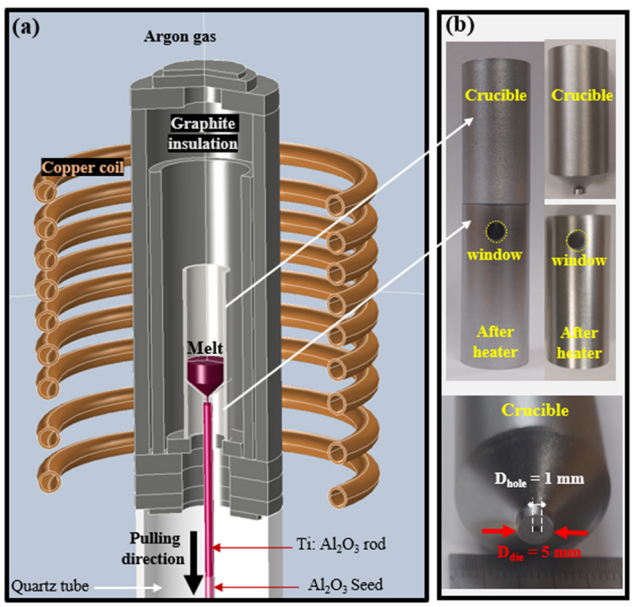

Fig. 2 (a) Schematic representation of the micropulling-down (μ-PD) furnace used for crystal growth, showing the main components of the setup and the downward pulling direction. (b) Photographs of the crucible and after-heater, highlighting the capillary die and its diameter (D_{die} = 5 mm) located at the bottom of the crucible, the die hole and its diameter (D_{hole} = 1 mm) and the observation window used for *in situ* monitoring of the growth process.

structural perfection and smooth surface quality. Further details on the μ-PD setup and general growth procedure can be found in our previous publications.[26,27,29,55,56]

3. Czochralski growth of Ti:sapphire crystals ($D \sim 30$ mm)

High-quality Ti:sapphire single crystals, weighing approximately 330 g with a diameter of 30 mm and a length of 125 mm, were successfully grown using the Czochralski (Cz) method, as illustrated in Fig. 1b. The overall configuration of the Cz crystal growth furnace is presented in Fig. 3a, showing the main components of the setup and the upward pulling direction used during the growth. This process required approximately one week for completion. Key parameters including a pulling rate of 1.5 mm h^{-1} and a rotation rate of 8 revolutions per minute (rpm) were adjusted during the experiments. Under optimized thermal gradients and stable convection flow, the resulting crystals exhibited high optical quality, as shown in Fig. 1b. The starting raw materials consisted of high-purity alumina (α-Al_2O_3) and titanium dioxide (TiO_2, rutile) powders. The alumina powder, supplied by RSA Le Rubis,[30] had a purity of at least 99.99%. These materials were loaded into a 60 mm-diameter crucible, which served as the container for the melt. The crucible was inductively heated by a water-cooled copper RF coil, as shown in Fig. 3a. To ensure uniform temperature distribution and stable thermal gradients, the RF coil, isolator system, crucible, and seed holder were precisely aligned along the same vertical axis. The entire growth process was carried out in a high-purity argon atmosphere at a pressure of 1 bar to prevent oxidation or other damage to the crucible and the crystal. Prior to heating, the furnace chamber was evacuated for one hour to remove residual gases and moisture, after which it was filled with argon to maintain an inert environment throughout the experiment. The charge materials were gradually heated until fully melted to form a homogeneous mixture. The seed crystal was then brought into contact with the free surface to initiate growth. The necking-down stage was first conducted to suppress the propagation of dislocations from the seed, followed by the shouldering stage, where the crystal diameter was slowly increased to the desired size. The tailing phase concluded the process by gradually increasing the temperature to reduce the diameter and separate the crystal from the melt. Controlled cooling to room temperature was employed to prevent cracking and internal stress.

An automatic diameter control (ADC) system, based on the time derivative of the crystal weight, was used to precisely maintain the crystal diameter during the entire growth process. To monitor melt decomposition and evaporation losses, the total weight of the crucible and charge was continuously measured throughout the experiment. More information about the growth process can be found in ref. 30.

4. Growth of large Ti-doped sapphire crystals ($D \sim 260$ mm)

Taking advantage of the optimization studies performed by S. Zermout *et al.*,[46,47] where a global numerical model of the large sapphire growth furnace was developed using a bottom resistive heating configuration beneath the crucible, a new growth furnace was designed for the present study. This apparatus was specifically optimized for large-diameter ($D \approx$ 260 mm) titanium-doped sapphire (Ti:Al_2O_3) crystal growth.

In this setup, large Ti:sapphire boules with 260 mm diameter and 270 mm height were successfully grown like the one shown in Fig. 1c. The growth was performed in a resistive furnace equipped with resistor heaters and a large

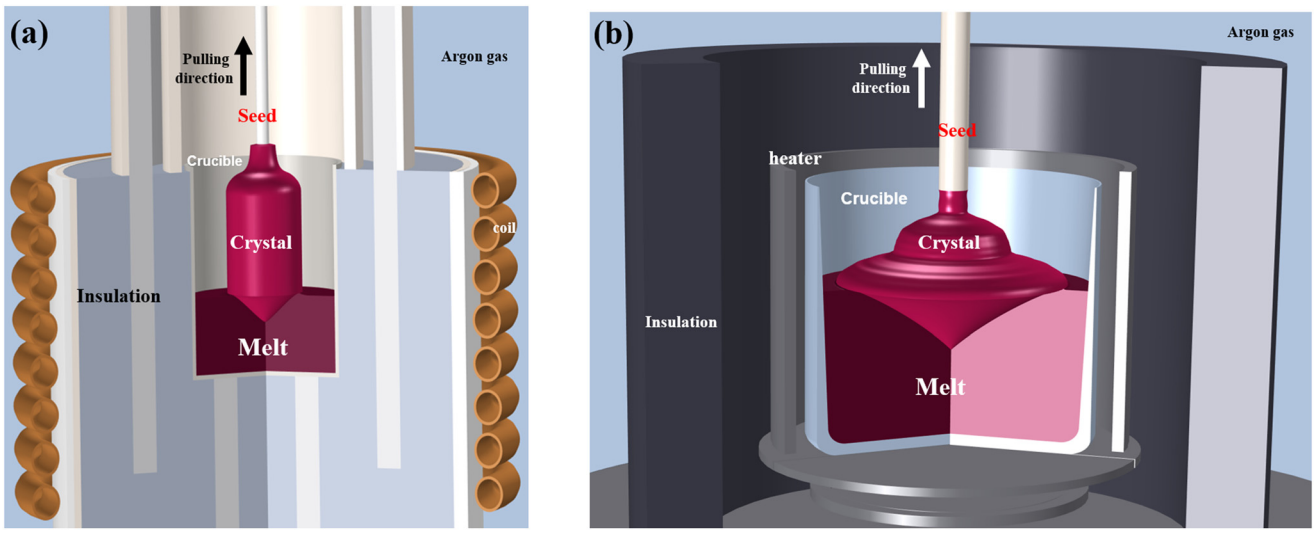

Fig. 3 Schematic representation of the crystal growth furnaces used for the growth of (a) medium (D = 30 mm) and (b) large ($D \sim$ 260 mm) titanium sapphire crystals, showing the main components of the setup and the upward pulling direction.

crucible (D = 300 mm, H = 312 mm) with a bottom round shape like presented in Fig. 3b. Surrounding the crucible, an insulation assembly was incrementally designed through several tests run with the aim of improving the symmetry of radial and axial thermal gradients, thus improving crystal shape and quality.

As starting materials, sapphire crackle and pellets of TiO_2 doped Al_2O_3 were used. Even though it can't be perfect due to the tedious nature of the task, particular care should be addressed to center every component inside the furnace like the crucible and the heaters to avoid any asymmetrical artefact on the global thermal field that would impact crystal growth negatively. Once the furnace is ready to run, two atmosphere cleaning cycles were conducted using a vacuum pump unit and argon gas. When 10^{-4} mbar is achieved, the furnace is filled with argon until atmospheric pressure is reached. The goal here is to remove as many parasite gases as possible, especially oxygen naturally present in the air and water due to humidity that is adsorbed by all the furnace components. After this step, a final vacuum to the same value is performed while the heating power of the sapphire raw material load is gradually increased to approximately 25 kW to help vaporize any moisture in the furnace while preventing raw materials from melting. Then argon is injected again, and the power is increased again to reach 45 kW so we can melt alumina raw materials. It was maintained for several hours, until convection lines become visible thanks to the camera, mounted on top of the furnace offering a view of the crucible centre indicating that the material has fully melted. Then, an *a*-axis sapphire seed crystal was carefully lowered to come into contact with the melt's free surface and initiate crystal growth. Using a mass feed-back system, the power is gradually decreased automatically to reach the user set crystal growth rate target.

5. Bubbles in the μ-PD Ti:Al_2O_3 sapphire rod with a fvery small diameter ($D \approx 5$ mm)

Numerical simulations of sapphire crystal growth by the micro-pulling-down (μ-PD) method were conducted using a comprehensive global finite element model. The model accounts for heat conduction in solid components, buoyant and forced convection in the melt and surrounding atmosphere, thermocapillary (Marangoni) convection at the melt free surface and meniscus, internal radiation within semitransparent regions (melt, crystal, quartz tube), and surface-to-surface radiation between exposed surfaces separated by argon gas. The simulated furnace geometry reproduces actual component dimensions, while experimental parameters such as rod diameter and length, seed diameter, and meniscus height replicate the configurations investigated experimentally. The detailed mathematical formulations, numerical implementation, and model validation are reported in our previous work.[55]

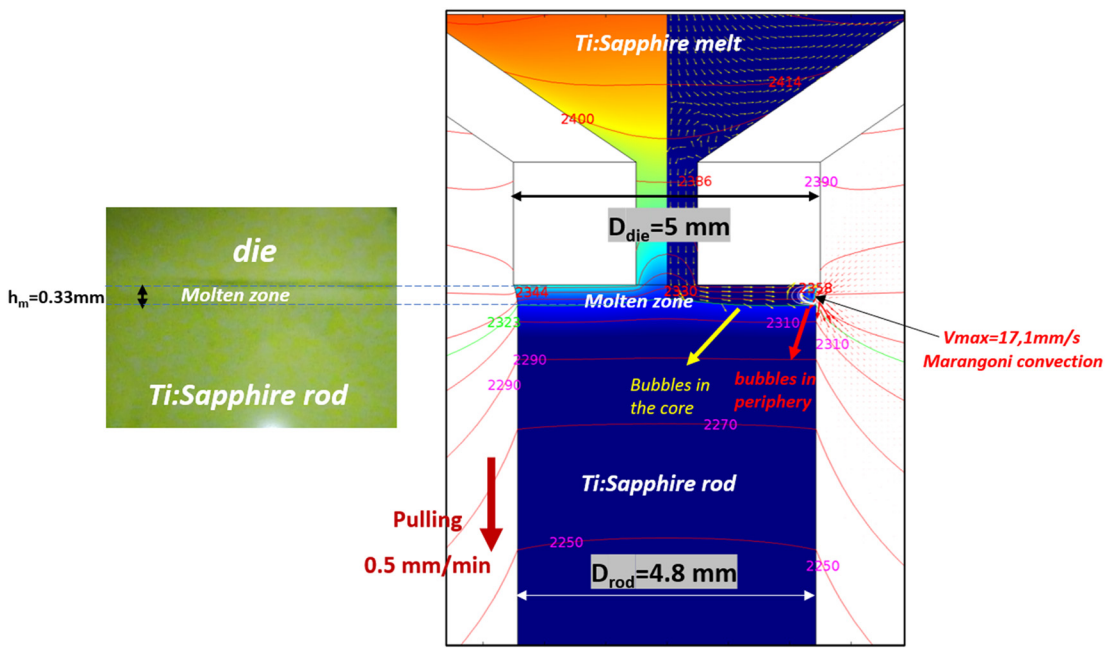

Fig. 4 Photograph captured from the observation window of μ-PD crystal growth schematized in Fig. 2, showing the bottom of the die (D_{die} = 5 mm), molten zone, meniscus ($h_m \approx 0.33$), and the most recently grown crystal ($D_{rod} \approx 4.8$ mm) at a pulling rate of 0.5 mm min^{-1} (left). The temperature field is plotted in the sapphire rod and molten zone and a part of the growth atmosphere; red arrows: velocity vectors in the gas near the meniscus; normalized yellow arrows: velocity vectors in the melt. Green line: isotherm at the melting temperature T_m = 2323 K. Forced convection induced by rod pulling driving bubbles from the molten zone toward the crystal center and Marangoni convection close to the meniscus are the main reasons of the bubble occurrence in the core of the crystal and at the crystal periphery, respectively.

Fig. 4 (left part) presents the μ-PD observation through the furnace window, showing the die (D_{die} = 5 mm), molten zone, meniscus (h_m = 0.33 mm), and the most recently grown crystal (D_{rod} = 4.8 mm). Fig. 4 (right part) illustrates the corresponding temperature and velocity fields: red arrows denote gas velocities near the meniscus, yellow arrows represent melt velocities, and the green contour indicates the isotherm at T_m = 2323 K. Rod pulling induces central bubble motion through forced convection, whereas Marangoni stresses promote bubble accumulation near the periphery. The overall melt flow remains weak due to the stabilizing thermal stratification, with the upper melt region being hotter than the die bottom, thereby suppressing buoyancy effects despite significant axial gradients.[50,53,55] Consequently, Marangoni convection governs the dominant flow pattern at the free surface.

Within the capillary region (D_{hole} = 1 mm), the downward pulling motion (V_{PL} = 0.5 mm min^{-1}) drives the transport of bubbles and impurities across the melt–crystal interface. The thin molten zone minimizes buoyancy-driven motion, confining thermocapillary flow to a ~200 μm layer adjacent to the meniscus. The flow intensity is quantified by the Marangoni number expressed by

$$M_a = \left|\frac{\partial\sigma}{\partial T}\right| \frac{\Delta T L}{\mu a} \quad (1)$$

where $\frac{\partial\sigma}{\partial T}$ is the temperature coefficient of surface tension, ΔT is the temperature difference along the meniscus, L is the characteristic length equal to the meniscus height here, μ is the dynamic viscosity, and α is the thermal diffusivity of the melt. A higher Marangoni number indicates a stronger surface-tension-driven flow.

Large bubbles present in the crucible after melting (>100 μm) rise due to the Archimedes buoyancy force:

$$F_b = \rho g V_b \quad (2)$$

where ρ denotes the melt density, g the gravitational acceleration, and V_b the bubble volume. These "relatively" large bubbles escape through the upper free surface of the melt (~4 mm^2) due to their large volume and also the capillary blocks re-entry, while stable stratification and weak surface flow facilitate their removal. In contrast, micrometric bubbles (10–70 μm) remain trapped within the melt.

In this study, the crystal diameter (D_{rod} = 4.8 mm) is slightly smaller than the die diameter (D_{die} = 5 mm), yielding a gently curved meniscus with a height of h_m = 0.33 mm and an almost planar solid–liquid interface exhibiting slight central convexity (<0.1 mm). The calculated Marangoni number is Ma = 560, with a maximum surface velocity of 17 mm s^{-1} near the meniscus. The pronounced outer Marangoni shear promotes peripheral bubble accumulation.

Fig. 5a shows the vertical velocity distribution of molten sapphire along the die-hole bottom radius for pulling rates between 0.25 and 5.0 mm min^{-1}. Due to the no-slip condition at the die wall, velocities are zero at the boundary and maximum at the centerline. The central downward velocity increases nearly linearly with the pulling rate, from approximately 14 mm min^{-1} at 0.5 mm min^{-1} to nearly 140 mm min^{-1} at 5.0 mm min^{-1}. Consequently, bubbles are transported toward the central region of the solidification front, accounting for the higher bubble density observed in

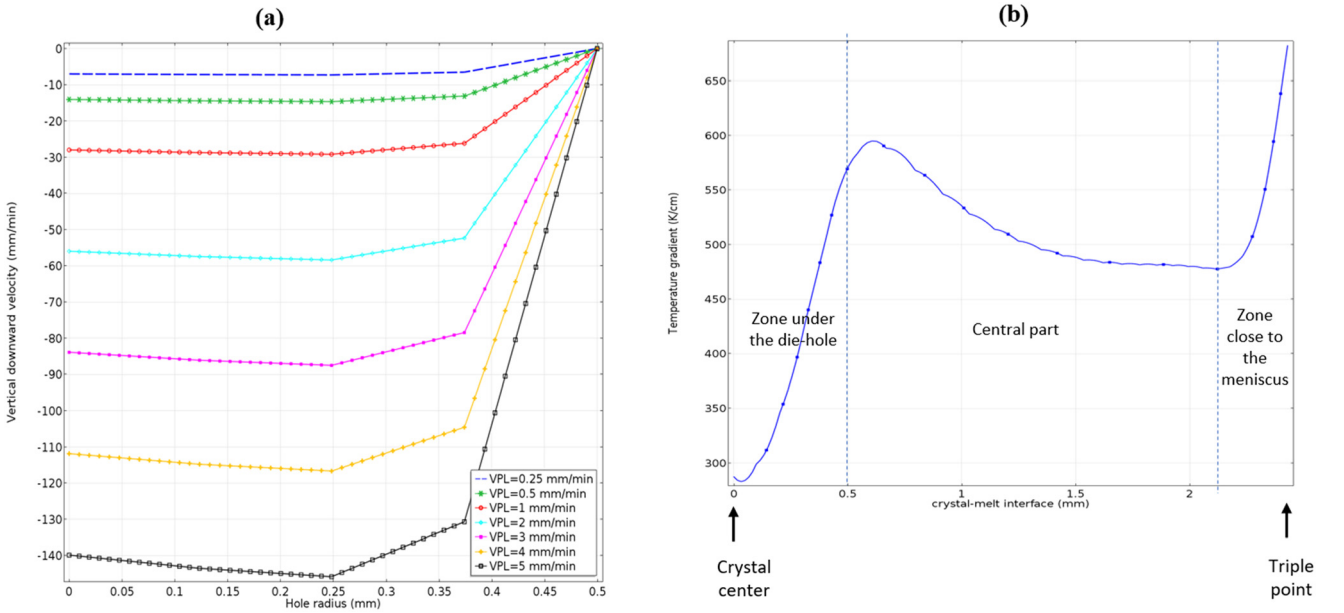

Fig. 5 Vertical downward velocity of molten sapphire at the exit of the die along the hole radius (a) for pulling rates: 0.25 mm min^{-1}, 0.5, 1, 2, 3, 4 and 5 mm min^{-1} (left plot). (b) Temperature gradient along the rod–melt interface. Relatively small gradient at the central part of the crystal under the die-hole and larger gradients close to the meniscus up to 670 K cm^{-1}.

the crystal core. At the lowest pulling rate (0.25 mm min^{-1}), the central downward velocity reduces to 7 mm min^{-1}, explaining the lower bubble concentration in the initial portion (0.5 mm) of the rod grown at this rate.

The flow regime remains laminar, as confirmed by the Reynolds number (Re):

$$\mathrm{Re} = \frac{\rho U D_{\mathrm{rod}}}{\mu} \quad (3)$$

For D_{rod} = 5 mm and $U = V_{\mathrm{PL}}$ = 0.5 mm min^{-1}, Re = 0.0216, decreasing by half at 0.25 mm min^{-1}. As Re $\ll$ 1 in all cases, the flow remains laminar. Despite the low Reynolds number, the downward flow is sufficient to carry micrometric bubbles toward the crystal–melt interface, where their small volume prevents buoyant rise as predicted by eqn (2). These bubbles are subsequently entrapped in the crystal, as depicted by the yellow velocity vectors going through the crystal–melt interface in Fig. 4.

A high temperature gradient near the solid–liquid interface is one of the most critical aspects of the μ-PD technique. This gradient strongly influences growth stability. However, it may also enhance dopant incorporation, potentially increasing bubble formation. During μ-PD growth of sapphire, the gradient at the temperature melt–rod interface is particularly steep, consistent with findings by Rudolph *et al.*[57] and Fang *et al.*[51] Reported gradients reach approximately 1000 K cm^{-1} for μ-PD growth of sapphire/YAG eutectic fibers,[57] while Fang *et al.*[51] observed values ranging from 600 to 1200 K cm^{-1}, depending on the thermal insulation thickness. In the present study, the calculated temperature gradient ranges from approximately 270 K cm^{-1} at the center of the interface to about 680 K cm^{-1} near the meniscus (Fig. 5b). This pronounced gradient enhances bubble transport from the melt into the growing crystal, contributing to the observed microstructural characteristics of μ-PD-grown sapphire.

The numerical predictions outlined above correlate strongly with the experimental results obtained for Ti:Al_2O_3 sapphire rods of small diameter ($D \approx 5$ mm). To analyze the distribution and morphology of bubbles within the Ti:Al_2O_3 crystals, optical microscopy was performed using transmission and reflection illumination. Magnifications of ×5, ×10, and ×20 were employed. The microscope was equipped with a digital video camera connected to a computer for image acquisition and quantitative analysis using dedicated software.

Fig. 6 presents micrographs of the titanium–sapphire rod at various positions along its length: (1) an initial region (≈500 μm) near the seed, free of bubbles, followed by a zone containing small spherical bubbles (≈10 μm); (2) typical spherical bubbles with diameters ranging from 10 to 90 μm, along with elongated bubbles aligned along the growth axis, and regions showing titanium traces around the bubbles, (3) smaller bubbles (≈10 μm in diameter) located near the rod extremity. According to previous studies,[25,26] undoped sapphire rods grown by the μ-PD technique typically exhibit bubbles with diameters of approximately 8 μm. Upon titanium doping, both bubble size and morphology are markedly altered.

The initial ~500 μm segment, corresponding to the manually controlled start-up phase, with a deliberately reduced pulling rate, shows a very low density of small bubbles (Fig. 6.1). This observation is attributed to the low growth rate during manual initiation, which allows bubbles to escape more efficiently. This experimental trend is in full agreement with the simulation results, which showed that at the lowest pulling rate (0.25 mm min^{-1}), the downward velocity of the melt (7 mm min^{-1}) is too small to drag bubbles into the interface, allowing buoyant (Archimedes force) release instead.

In the following ~500 μm region, the 10 μm spherical bubbles are observed at low concentrations compared to the rod end (Fig. 6.3). Their morphology is similar to that found in undoped sapphire grown under comparable conditions,[26,55] reflecting the low initial Ti concentration in the melt zone, which remains in contact with the undoped seed. In the central portion of the rod, where Ti concentration is greater, bubbles become larger and morphologically diverse (Fig. 6.2). Both spherical and irregularly shaped bubbles are present, with diameters up to

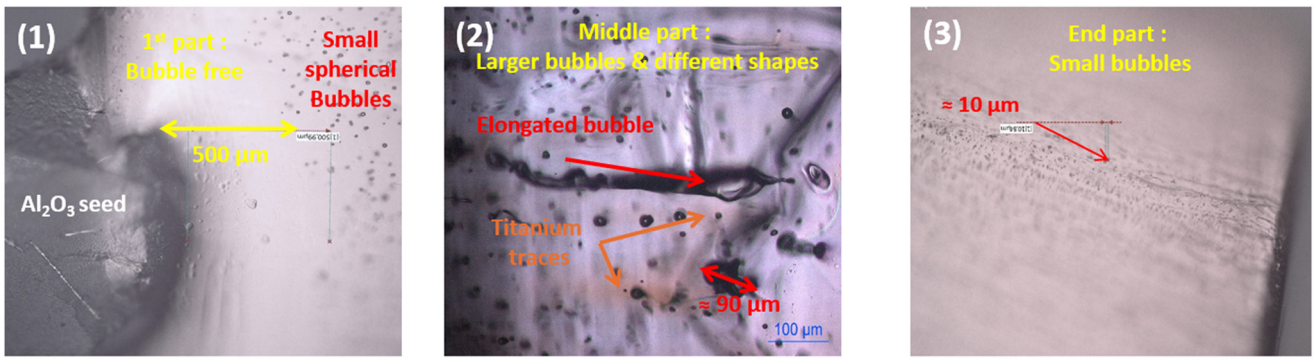

Fig. 6 Micrographs of the titanium–sapphire rod at different positions: (1) an initial small region (≈500 μm) near the seed, free of bubbles, followed by an area containing small spherical bubbles; (2) typical spherical bubbles of various sizes (10–70 μm), elongated bubbles within the rod and regions showing titanium traces around bubbles; (3) smaller bubbles (≈10 μm in diameter) located near the end of the rod.

90 μm, while elongated bubbles aligned along the growth direction can extend up to 300 μm in length. This evolution is directly correlated with the presence of Ti^{3+}/Ti^{4+} species in the melt, which significantly influence gas entrapment, melt viscosity, and bubble dynamics during crystallization. These observations correspond well to the simulated flow fields, which predict intensified downward convection and stronger thermocapillary shear at higher pulling rates, both of which favor bubble trapping along the growth axis.

Toward the end of the rod (Fig. 6.3), average bubble size decreases substantially. The remaining bubbles are predominantly spherical, with diameters around 10 μm. This reduction is consistent with the gradual depletion of Ti in the melt during the final growth phase, resulting in conditions like those at the start of the process.

Finally, the systematic variation in bubble morphology and size along the rod clearly demonstrates the strong interaction between titanium concentration, melt stability, and gas incorporation during the μ-PD growth of $Ti:Al_2O_3$ sapphire crystals. The close agreement between numerical predictions and experimental observations confirms that bubble entrapment is governed by a combination of pulling-induced convection, Marangoni effects, and the evolution of Ti concentration in the melt.

6. Bubbles in medium-sized crystals ($D \approx 30$ mm)

When the entire charge of titanium-doped sapphire is completely melted, it contains a significant number of gas bubbles of different scales. At the initial stage of Czochralski (Cz) growth, as for the μ-PD process, large bubbles are predominantly located in the upper part of the melt. Under the influence of Archimedes' force, these bubbles rise naturally toward the free surface of the melt which is wider for the CZ process. Since this force is proportional to the bubble volume, larger bubbles ascend more rapidly, while smaller (micrometric) ones remain entrained within the convective flow of the melt, which is governed by the combined effects of natural and Marangoni convection and also by forced convection induced by crystal rotation and crystal pulling. In contrast to the μ-PD process, the stronger buoyant forces characteristic of the CZ configuration favor the upward displacement of bubbles along the crucible sidewall, promoting their efficient evacuation through the free surface.

To characterize bubble morphology, distribution, and their effect on optical quality, the CZ Ti:sapphire crystal (Fig. 1b) was cut into 5 mm wafers perpendicular to the growth direction.[24] Three wafers were selected from the top (seed region), middle, and tail, and subsequently optically polished for microscopic examination. In 30 mm-diameter $Ti:Al_2O_3$ crystals grown by the Cz method, bubbles typically range between 10 and 45 μm in diameter.[24] They appear as isolated spheres, irregular coalesced clusters, or well-aligned chains parallel to the growth axis. Their axial distribution exhibits a characteristic three-zone pattern: a high bubble density near the seed end, a long central region that is virtually bubble-free, and a reappearance of dense bubble clusters near the tail. This pattern is governed by titanium segregation. As the growth proceeds, Ti^{3+} ions rejected from the solid phase accumulate in the melt, enhancing constitutional supercooling near the end of the process and leading to morphological breakdown of the interface. The resulting cellular or dendritic protrusions act as preferential sites for heterogeneous bubble nucleation and trapping.[31] Fig. 7 shows the distribution of bubbles observed at the top (near the shoulder), in the middle (cylindrical region), and at the bottom (tail) of a Ti-doped sapphire ingot grown by the Czochralski technique. No bubbles were recorded in the cylindrical region. In contrast, the beginning of the crystal contains a few bubbles. In the tail region, the bubble density increases significantly. At the beginning of growth, bubbles may result from the dissociation of molten alumina. Small bubbles can also form due to supercooling of the melt below the solid–liquid interface. Furthermore, during the early growth stage, bubble kinetics are influenced by the melt temperature and the concentration of dissolved gases in the melt. Therefore, the effect of Ti segregation is limited during the seeding stage.

Fig. 7 Bubble distribution as a function of position in a Ti-doped sapphire crystal grown by the Czochralski (CZ) technique: (a) beginning of the ingot (near the shoulder), (b) cylindrical region (middle of the ingot, bubble-free), and (c) end of the ingot (tail region) showing agglomerated bubbles.

At the end of growth, more Ti dopant is rejected into the melt due to segregation, leading to an increase in bubble density (Fig. 7c). Because of Ti segregation at the melt–crystal interface, bubbles tend to agglomerate around Ti-enriched regions. In the tail region, optical microscopy revealed characteristics consistent with destabilization of the solid–liquid interface caused by solute accumulation.

A comprehensive finite element model was developed to simulate the temperature distribution and fluid flow within the Cz furnace. The model incorporated all relevant physical processes, including electromagnetic heating, heat conduction in solid components, buoyant and thermocapillary convection in the melt and gas phases, internal radiation within the melt and the crystal, radiative heat exchange through the surrounding argon atmosphere, and crystal rotation and pulling. The furnace geometry reproduced the experimental configuration, with a crystal diameter of 30 mm and a crucible diameter of 60 mm. Numerical results (Fig. 8) revealed that the melt–crystal interface is convex toward the melt, with an interface deflection of approximately 8 mm. This convexity results from the combined effects of surface radiation, buoyant and forced convection, with internal radiation in the semi-transparent crystal and melt playing a dominant role.

The simulation predicted a temperature difference of ΔT = 160 K within the melt and a surface temperature variation of ΔT_s = 123 K. The Grashof number ($Gr = g\beta\Delta TL^3/\nu^2 \approx 2.0 \times 10^5$) confirms that the melt remains in the laminar convection regime, since transition to turbulence occurs near ($Gr \approx 10^8$). Using an effective characteristic length L = 1.5 cm for surface convection, the Marangoni number expressed in (1) was calculated as ($Ma \approx 7.3 \times 10^4$), indicating thermocapillary activity at the melt surface, secondary to buoyant forces but still significant in shaping surface flow. For a crystal rotation speed of 8 rpm, the corresponding Reynolds number is $Re \approx 98$, confirming laminar forced convection.

The maximum velocity within the melt reaches approximately 3.3 cm s^{-1}, occurring near the free surface of the melt, where a stable toroidal vortex transports heat from the crucible wall toward the crucible center. This steady, laminar circulation minimizes thermal fluctuations and compositional inhomogeneities, while the downward jet along the axis enhances heat extraction and contributes to the convex shape of the interface. Radiative heat exchange, combined with sapphire's semitransparency, further modulates the interfacial curvature.

In addition, the upward flow of fluid particles near the crucible sidewall helps the bubbles to move upward and escape from the melt free surface. The intensity of this upward flow reaches 6 mm s^{-1} and can be strongly efficient to displace the bubbles upward from the bottom toward the free surface.

The temperature gradients at the crystal–melt interface in the CZ process, ranging from 150 K cm^{-1} at the center to 300 K cm^{-1} near the triple point (Fig. 8b), are lower than those

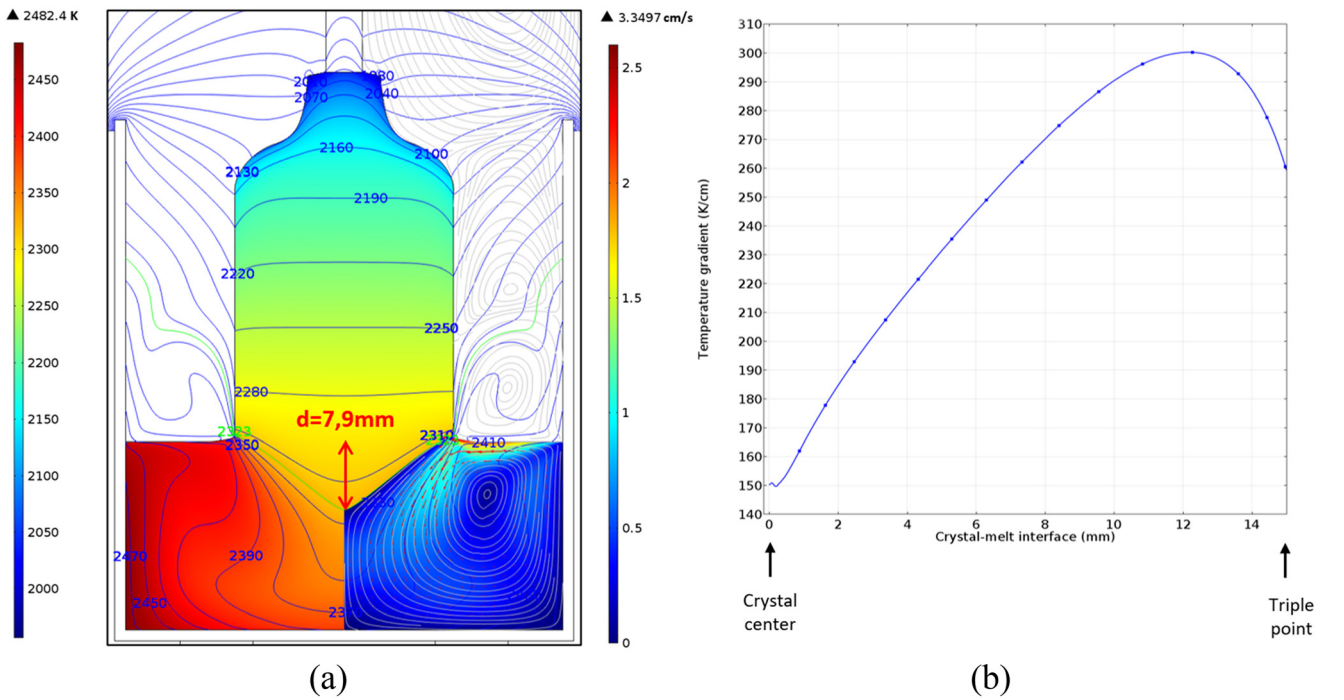

Fig. 8 Numerical simulation results displaying (a) the velocity field (right) and temperature field (left) for the 30 mm diameter titanium-sapphire crystal grown in the inductive Czochralski process presented in Fig. 3a. Isotherms indicate temperature distributions within the crystal, the melt, and the surrounding argon atmosphere. Red arrows represent velocity vectors in the melt, and the green line denotes the melting-point isotherm (T_m = 2323 K). The deflection of the convex crystal–melt interface is d = 7.9 mm. (b) Temperature gradient along the crystal–melt interface.

observed in μ-PD growth. This difference provides one explanation for the reduced bubble density in Cz-grown Ti:sapphire crystals. Furthermore, the larger free surface area in the Cz method, bounded by the crucible (diameter 60 mm) and the crystal (diameter 30 mm), significantly enhances bubble removal. In contrast, the μ-PD process, characterized by a meniscus height of only ~0.3 mm, restricts the escape of gas bubbles, leading to their entrapment within the growing rod.

7. Bubbles in large titanium sapphire crystals ($D \approx 260$ mm)

Numerous challenges must be addressed during large crystal growth, such as maintaining the crystalline orientation throughout the process, ensuring homogeneous dopant distribution despite possible segregation, and, most critically, preventing inclusions, particularly gas bubbles, which can severely degrade the optical and mechanical quality of the grown crystal for laser amplification chain applications. Characterizing the density, nature, shape, and location of these bubbles within the crystal provides essential insight into their formation mechanisms and movement through the melt before becoming trapped at the solid–liquid interface.

Typically, studying bubbles in large sapphire single crystals requires cutting and polishing the grown ingot, since direct observation is difficult due to the high refractive index contrast between air (n = 1.002[58]) and sapphire (n = 1.774[1]) at room temperature combined with the irregular ingot surface state and crystal thickness. The larger the ingot, the more challenging and labor-intensive this process becomes. This explains why investigating bubble defects within bulk sapphire ingots remains difficult and why only limited studies addressing such defects in large sapphire single crystals are available in the literature.[23,59] As the crystal has a smaller diameter on the top part, it is easier to look directly inside in ambient air. We can then appreciate inside the crystal's top part by looking through regular surface state areas (like facets). We can identify qualitatively under strong white light, some macroscopic defects with indications on their morphology (approximate size and shape) like inclusions (bubbles or solid particles) and global distribution in the Ti:sapphire ingot top part (Fig. 9), but it is difficult to see through the remaining part on these conditions. To better see inside the whole crystal without cutting it, an approach consisting of reducing the refractive index gap between sapphire and air can be chosen. For that, the crystal is immersed inside different media with a higher refractive index than air and lower than the one of sapphire. The first easy and cheap solution to set up is to fill a glass tank with tap water (n = 1.366[60]), put the sapphire crystal inside and observe. With this technique, we better see inside the crystal, and the tendencies seen before can be confirmed but better can be done.

To further enhance the inspection process, the crystal was immersed in diiodomethane (n = 1.746[61]), in the TotalScan® equipment. This medium has a refractive index that closely matches that of sapphire. This procedure revealed the same features (yellow circle in Fig. 10) observed when using water and in air, but with significantly greater clarity. An arch like bubble shape can be distinguished in air, better seen in water and totally seen in diiodomethane. The small refractive index difference between diiodomethane and sapphire allows us to see through the crystal while still clearly distinguishing its overall shape.

Under polarized light in extinction mode, the c-axis (perpendicular to the growth direction) can be identified by the characteristic cross-shaped interference pattern visible along the entire crystal length, indicating that the orientation was well preserved throughout the growth process. However, due to the surface condition of the crystal, this optical pattern alone on the bulk sapphire ingot does not provide conclusive information regarding its crystalline quality.

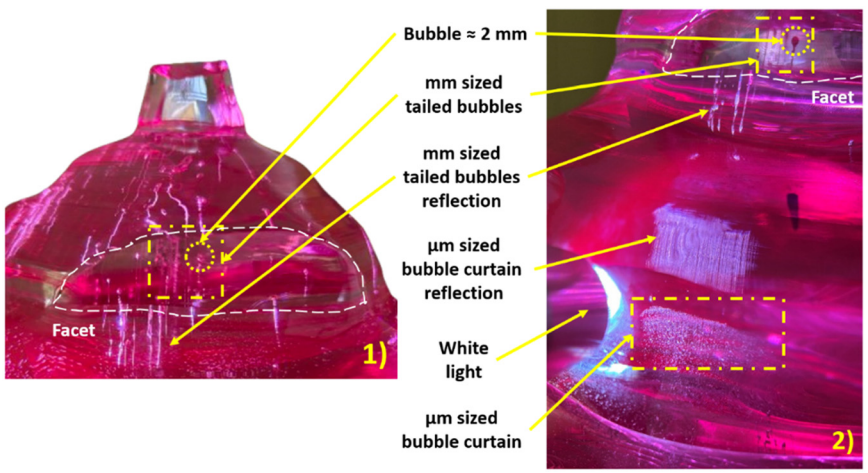

Fig. 9 Different inclusion sizes and shapes in the large Ti:sapphire crystal. 1) In the top part. 2) Same defects observed in the top part but with additional view on the middle part.

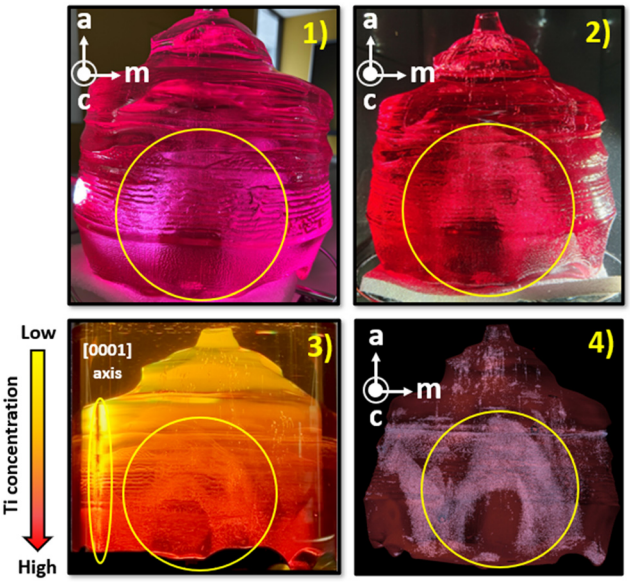

Fig. 10 1) Qualitative visual inspection of the same crystal presented in Fig. 1 with the same placement: 1) under strong withe light in air, 2) under strong white light in water, 3) under strong polarized light in a high refractive index media (the *c*-axis and thus the *m* axis are shifted by a slight rotation of the crystal to the left to observe both the interference pattern and the bubble arch like shape, 4) 3D model of scattering points inside the crystal captured by the TotalScan equipment.

Additionally, titanium segregation is observed as a red color gradient extending from the top to the bottom of the crystal. This variation is particularly noticeable and relevant in the region of stable diameter, where the color gradually changes, truly indicating titanium segregation. On a more quantitative scope, the equipment is also able to capture crystal shape, dimensions and scattering point positions inside the crystal within the detection limit in between 7 and 10 μm. Unfortunately, the scanning itself did not give us any information on defect nature in our case, but it can give information on global morphology. In Fig. 10, the whole titanium doped sapphire 3D model is shown with its captured scattering points. Different defect distribution is shown whether at the top part or the rest of the ingot. In fact, the crystal scan top part shows tailed scattering points with a spherical shape on its upper part which is in good agreement with the millimeter tailed bubbles seen previously in Fig. 9.

The scattering points inside 10 mm crystal slices are plotted along the reference axis to gather more information on localized areas. Along with the growth axis (*a* axis), the ingot starting from the bottom to the top is sliced. Fig. 11 shows one slice with its scattering points and its position within the crystal. An axisymmetric bubble ring can be clearly identified at this position at 150 mm from the crystal's bottom part perpendicular to the growth direction.

A comprehensive global finite element model was developed to compute the temperature distribution throughout the entire furnace and the velocity fields in both the melt and the surrounding gaseous atmosphere. The model incorporates all relevant heat and mass transfer mechanisms inside the system, including heat conduction in solid components, buoyant and forced convection in the melt and atmosphere, thermocapillary (Marangoni) convection at the melt's free surface, internal radiation within the semi-transparent crystal and melt, and surface-to-surface radiation between components separated by argon gas. The furnace geometry was reconstructed to match the actual dimensions

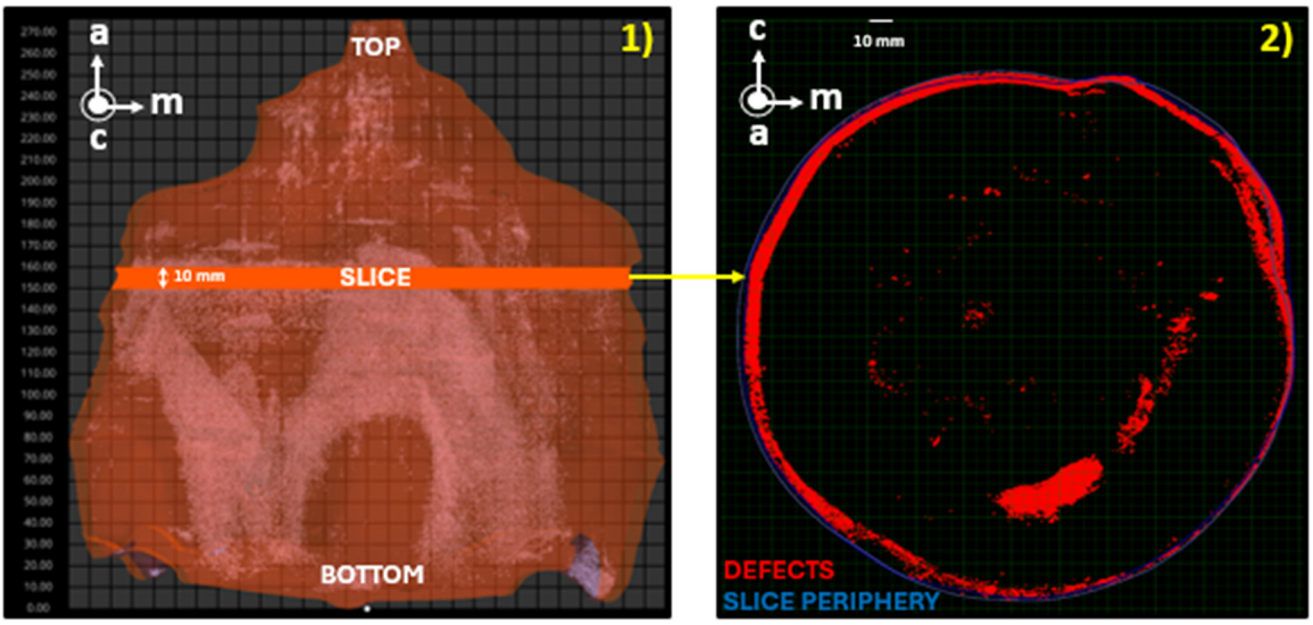

Fig. 11 1) Front view in orthographic projection of scattering points in 3D models inside the crystal obtained using TotalScan equipment; 2) 10 mm slice taken at 150 mm from the crystal's bottom part perpendicular to the growth direction with its top view to see defect distribution.

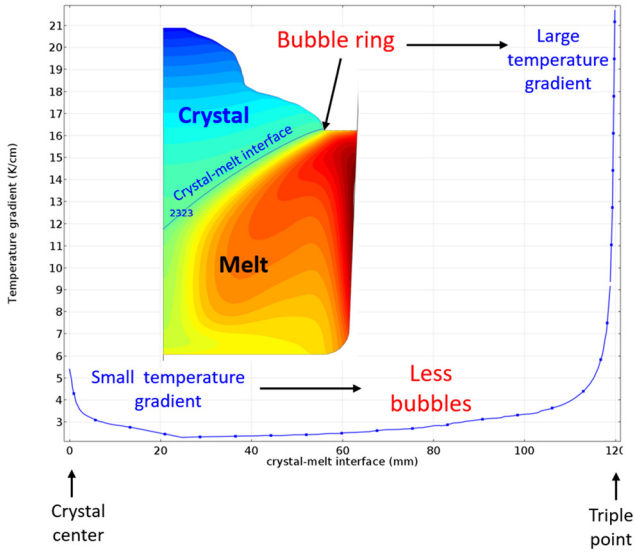

Fig. 12 Temperature gradient along the interface. Large values are found close to the triple point where a ring of bubbles is observed in the crystal.

of all components, ensuring close correspondence with the experimental setup.

Simulation results (Fig. 12 and 13.3) revealed that the crystal–melt interface during large-scale growth was highly convex toward the melt, consistent with previous experimental and numerical studies.[42,43,45–47] The curvature of the conical interface reached approximately 81 mm at the onset of the cylindrical growth stage, marking the transition from the initial conical portion to the steady-state cylindrical region. This pronounced convexity is a direct consequence of several coupled physical processes, with internal radiation within the semitransparent regions acting as the dominant contributor. The complex interaction between convective heat transport and radiative transfer shapes the temperature field and flow structure near the solidification front, thereby defining the interface geometry.

During this phase, the temperature gradients and melt flow near the crystallization front play a decisive role. The laminar flow regime is governed by the arrangement of heaters and insulation in the furnace, producing a temperature gradient of approximately 21 K cm^{-1} near the triple junction where molten sapphire, solid sapphire, and argon gas meet (Fig. 12). The maximum melt temperature reaches 2342.5 K, while the maximum free surface temperature is 2335 K, yielding a moderate vertical thermal gradient suitable for stable growth.

The flow regime was characterized using dimensionless parameters. The Grashof number is equal to $Gr = 3.11 \times 10^6$ which confirms laminar natural convection, since transition to turbulence typically occurs near $Gr = 10^8$ as said previously. Thus, buoyancy-driven flow in the large melt volume remains laminar and stable, a favorable condition for maintaining interface uniformity and suppressing compositional fluctuations that can be induced by turbulent eddies.

The Marangoni number, $Ma = |d\sigma/dT|\Delta TL/(\mu\alpha)$, gives $Ma = 1.19 \times 10^4$. This "relatively" small value indicates that thermocapillary forces are weak compared to viscous damping, consistent with the limited liquid–gas interface area in this growth configuration. As a result, Marangoni convection contributes only secondary enhancement to the overall flow, ensuring that buoyancy remains the dominant driver of circulation.

The furnace is heated from the sides and bottom, producing higher temperatures near the crucible wall compared to the central region. This temperature distribution generates a single, dominant toroidal vortex that transports heat from the hot sidewalls toward the cooler

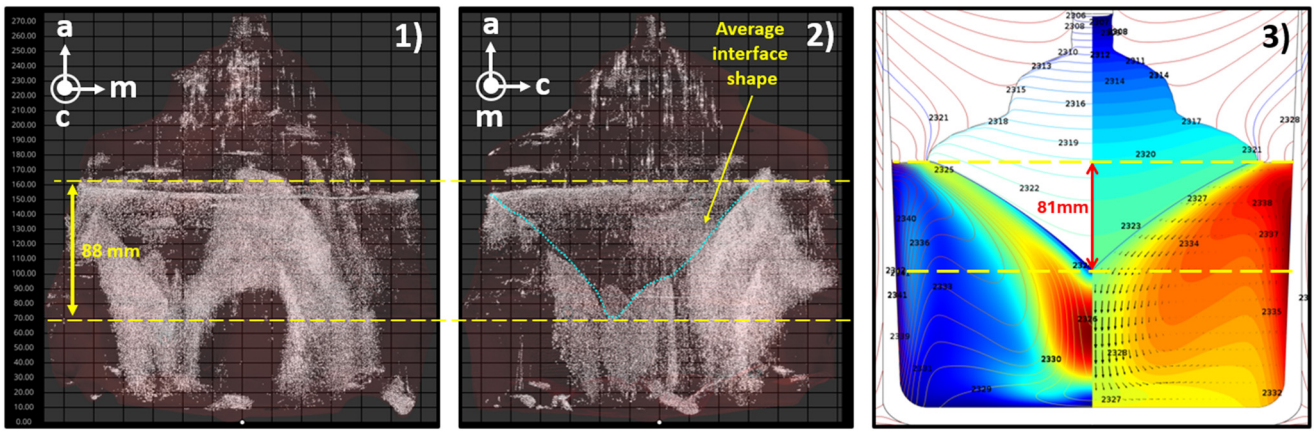

Fig. 13 (1 and 2) Front view in orthographic projection of scattering points in 3D models inside the crystal obtained using TotalScan equipment, shown from two orientations: (1) *c*-plane and (2) *m*-plane. (3) Numerical simulation results displaying the velocity field (left) and temperature field (right). Isotherms indicate temperature distributions within the crystal, the melt, and the surrounding argon atmosphere. Black arrows represent velocity vectors in the melt, and the blue line denotes the melting-point isotherm (T_m = 2323 K). The deflection of the conical crystal–melt interface is d = 81 mm. The distribution of bubbles observed in (1) and (2) is located just beneath an approximate conical surface almost equivalent to this deflection with a 87 mm height.

Table 1 Calculated temperature gradients at the solid–liquid interface, and flow regimes in Ti:Al_2O_3 growth systems

Growth method	Crystal diameter (D_c)	Characteristic length (L)	Dominant convection type	Temperature gradient at the interface (K cm^{-1})
μ-PD	5 mm	Meniscus height h_m = 0.33 mm	Marangoni	Max = 680 Min = 270
Cz	30 mm	Crucible diameter D = 30 mm	Buoyant + Marangoni + forced	Max = 300 Min = 150
Large-scale	260 mm	Crucible diameter D = 300 mm	Buoyant (weak than CZ)	Max = 22 Min = 2

interior and crystallization front. Hot, low-density fluid ascends along the crucible wall with relatively small velocities up to 2.4 mm s^{-1} at mid-height, while near the free surface the flow decelerates to about 1 mm s^{-1} due to weak surface-tension effects. A strong downward jet develops along the central axis, reaching 8.93 mm s^{-1} according to simulations. This descending motion arises from the cooling and densification of fluid parcels that release latent heat at the crystal–melt interface before sinking toward the crucible bottom.

The hydrodynamic behavior significantly influences bubble motion and crystal quality. Small gas bubbles, typically generated from residual impurities or melt decomposition, experience competing buoyancy and viscous drag forces. For microbubbles with radii about 10–100 μm, the terminal rise velocity estimated from Stokes' law, $V_b = 2R_b^2 g(\rho - \rho_b)/9\mu$, is only 0.1–1 mm s^{-1}.[62–65] This bubble velocity is substantially lower than the downward melt velocity, where R_b is the radius of the bubble, ρ is the density of the liquid and ρ_b is the density of the gas inside the bubble (usually $\rho_b \ll \rho$).

Consequently, most microbubbles are advected downward along with the melt flow, which prevents their entrapment at the solid–liquid interface and reduces internal defect density. Some bubbles may escape at the free surface or accumulate transiently near the crystal periphery, forming a ring-like pattern like the ring observed in Fig. 11. However, the majority follow the main convective trajectories, confirming the critical role of flow topology in defect mitigation.

The strong downward flow at the melt center enhances cooling efficiency near the interface, producing localized undercooling that accelerates growth in the central region and contributes to the formation of a highly convex interface. Radiative heat transfer and sapphire's semitransparency, combined with the furnace's heat shield configuration, further modulate the temperature field and thus the curvature of the interface. The predicted conical interface height (~81 mm) closely matches the experimentally observed bubble distribution zone (~87 mm) as clearly shown in Fig. 13, validating the model and confirming consistency between simulation and experiment. The minor discrepancy likely results from idealized boundary conditions and the 2D axisymmetric assumptions.

Comparison of the temperature gradients found at the crystal–melt interface (see Table 1) of this large crystal (260 mm diameter), plotted in Fig. 12, to the previous CZ and μPD crystals indicates that smaller values are found, 20 K cm^{-1} against 300 K cm^{-1} for CZ (30 mm diameter) and 600 K cm^{-1} for μPD rod (5 mm diameter). The reduced temperature gradient observed in large-diameter crystals stems from controlled radiative cooling *via* furnace heat shields, which sustains a submerged growth interface without mechanical pulling and promotes uniform, single-vortex melt convection.

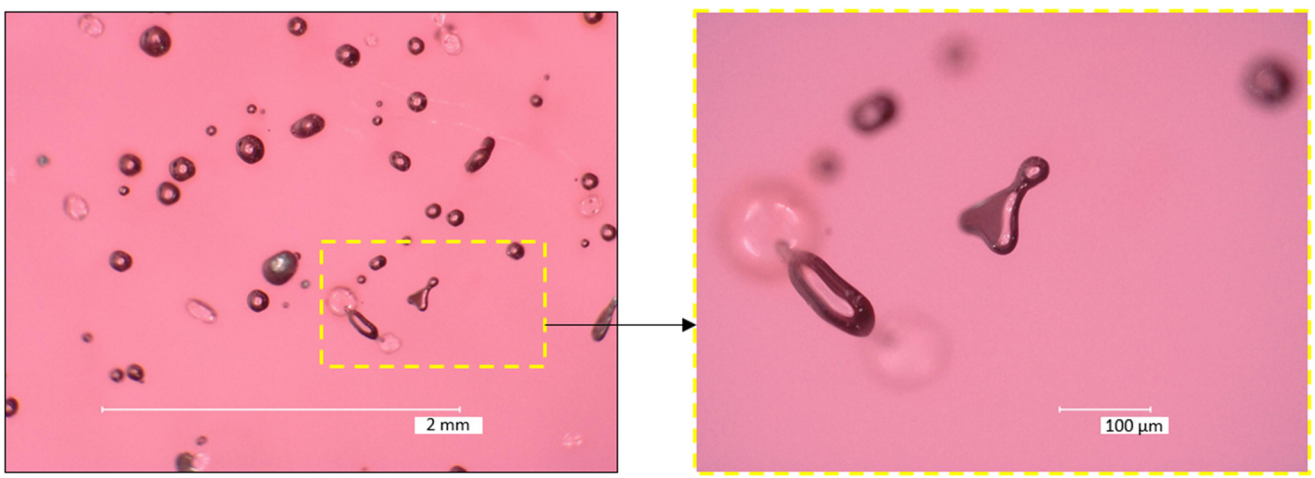

Fig. 14 Micrographs of the large titanium–sapphire crystal showing bubbles with different shape and size.

Table 2 Bubble morphology and distribution

Region/growth stage	Typical bubble diameter (μm)	Shape	Density/concentration trend	Cause
Small scale: μ-PD rod (D = 5 mm)				
Initial segment (≈0–0.5 mm)	<10	Spherical	Very low	Low pulling rate → gas escape
Central part	10–70	Spherical & elongated	High	Strong Marangoni + Ti concentration + pulling effect
Final part (≈10 mm)	~10	Spherical	Low	Ti depletion reduces trapping
Medium scale: CZ crystal (D = 30 mm)				
Top part	10–45	Irregular clusters	High Concentrated in the core	Gas entrapment during initiation
Middle part	—	—	None/very low	Large free surface & buoyancy
Tail part	10–30	Irregular	Moderate Concentrated in the core	Ti segregation
Large scale (D = 260 mm)				
Top part	200–3000	Spherical/tailed	Very high: visible to the naked eye	Surface trapping, low gradient
Beginning of cylindrical part	10–100	Spherical/tailed	Peripheral ring	Large temperature gradient at the triple point
Remaining	10–100	Spherical & elongated & other shapes (bean, heart…)	Different: conical & arch like bubble shape in the bottom	Conical interface &weak buoyancy & small free surface &Ti segregation

The expanded surface area of larger crystals further dissipates heat radially, diminishing the gradient and avoiding the steep profiles (300–600 K cm^{-1}) of CZ or μPD processes.

In the cylindrical region of the large-diameter-grown crystal (D = 260 mm), the ratio of the free melt surface area to crucible cross-section is substantially lower than in conventional CZ growth (D = 30 mm), reflected in crystal-to-crucible diameter ratios of 26/29 *versus* 30/60, respectively. This reduced free surface restricts gas evacuation from the melt, promoting partial bubble entrapment and incorporation into the crystal lattice. In contrast, the expansive free surface in CZ processes enables efficient degassing through buoyancy-driven advection and diffusion, accounting for the scarcity of bubbles in those crystals. Bubbles of different size and shape are present in the large titanium doped crystal as shown in Fig. 14. Spherical, elongated, and even "heart" or "bean" shaped bubbles of sizes from 10 to 200 μm have been found.

8. Bubbles from small to large scale

As discussed above, the characteristics of temperature gradients, convection regimes, and geometry effects strongly determine the behavior of bubbles during Ti:Al_2O_3 crystal growth. Changes in scale and growth method modify the dominant flow mechanisms, which in turn influence bubble size, morphology, and distribution within the solidified material.

The observed bubble structures reflect the fluid-dynamic conditions, as summarized in Table 2. From very small spherical bubbles (<10 μm) in the top part of μ-PD rods to millimetric bubbles (>3 mm) in the top part of large crystal with different intermediate size, shape and concentration in each scale and each part of the crystal. The mechanism of trapping or escape is different at each part of each crystal,

Table 3 summarizes the mechanisms governing these phenomena. Marangoni convection is most significant in μ-PD growth, driving bubble accumulation near the periphery. Buoyant convection predominates in the Cz

Table 3 Summary of dominant physical mechanisms influencing bubble behavior

Mechanism	Description	Most significant in	Effect on bubbles
Marangoni convection	Surface-tension-driven flow at melt surface	μ-PD	Peripheral bubble accumulation
Buoyant convection	Density-driven flow due to temperature gradients	Cz	Promotes bubble rise and escape when the free surface is sufficiently large
Forced convection	Flow induced by pulling or crystal rotation	μ-PD Cz	Enhances downward transport in μ-PD and upward transport in Cz
Radiative transfer	Internal and surface radiation shaping T-field	Large-scale Cz	Controls interface curvature
Ti segregation	Dopant concentration altering viscosity & gas solubility	All	Increases bubble size, distribution and trapping
Thermal gradient	Drives flow stability and interface morphology	All	Controls trapping and release dynamics

system, aiding bubble rise and escape. Forced convection caused by pulling or crystal rotation assists downward transport, particularly in smaller crystals leading to bubble concentration in the rod center. Radiative heat transfer becomes increasingly important in larger systems, affecting interface curvature and thermal-field uniformity. Ti segregation influences all scales by modifying melt viscosity and gas solubility, thereby altering bubble growth and retention. The temperature gradient remains a universal factor that controls flow stability and the morphology of the solid–liquid interface, ultimately determining bubble trapping and release efficiency.

9. Conclusion

The comprehensive experimental and numerical investigation of bubble behavior in Ti:Al_2O_3 sapphire crystals grown by the micro-pulling-down (μ-PD), Czochralski (Cz), and large-scale furnace methods reveals the fundamental mechanisms controlling gas entrapment across different growth scales. Finite element simulations incorporating heat conduction, convection, radiation, and thermocapillary effects provided quantitative agreement with experimental observations, validating the physical models governing fluid flow and bubble dynamics in molten sapphire.

In μ-PD-grown rods ($D \approx 5$ mm), the combination of strong thermal gradients (270–680 K cm^{-1}), limited molten zone volume, and small free surface area results in constrained bubble mobility. The pulling-forced convection (Re $\ll$ 1), Marangoni convection domination near the meniscus, drives peripheral bubble accumulation and central entrapment under forced convection. Reducing the pulling rate, meniscus height and Ti concentration can be proposed to reduce bubble density and size along the Ti:Al_2O_3 rod.

For medium-diameter Cz-grown crystals ($D \approx 30$ mm), buoyancy and forced convection become the primary transport mechanisms. The larger melt volume and wider free surface significantly enhance bubble evacuation efficiency, leading to a characteristic three-zone axial distribution: bubble-rich near the seed, bubble-free in the central section, and bubble-reappearance near the tail due to Ti segregation and constitutional supercooling. The lower interfacial temperature gradients (150–300 K cm^{-1}) and laminar melt flow (Gr $\approx 2 \times 10^5$, Ma $\approx 7 \times 10^4$) minimize gas trapping and promote higher optical quality compared with μ-PD growth.

In large-diameter crystals ($D \approx 260$ mm), the reduced temperature gradient (~20 K cm^{-1}) and stable toroidal vortex ensure uniform heat removal and compositional homogeneity. The weak thermocapillary effect (Ma $\approx 1.2 \times 10^4$) and small free surface area, however, limit gas escape, resulting in partial bubble entrapment near the periphery and within the highly convex interface region. The close correlation between the simulated interface curvature (~81 mm) and experimentally observed bubble zone (~87 mm) confirms the strong predictive capability of the used global finite element model.

Finally, the study demonstrates that bubble formation and entrapment in Ti:sapphire crystals are governed by the interaction of Marangoni, buoyant, and forced convective flows, modulated by growth geometry, thermal gradients, and dopant concentration. Scaling up from μ-PD to Cz and large-furnace growth progressively reduces temperature gradients and enhances melt stability, thereby mitigating bubble incorporation and improving crystal transparency. These insights provide a robust foundation for optimizing growth parameters to reduce gas inclusion quantity inside Ti:sapphire crystals thus improving the fabrication of high-optical-quality crystals for high-power laser applications.

Conflicts of interest

There are no conflicts to declare.

Data availability

All data generated or analyzed during this study are included in the manuscript (CE-ART-12-2025-001214). The datasets are fully presented within the figures and tables. No additional datasets were deposited in public repositories.

Acknowledgements

This work was supported by ANR Labcom "SaphirLab" research program and Idémo Auvergne Rhone Alpe Region (SEPO450). The authors thank CNRS (IRP CNRS "ScintLab" project) for their financial support and ANRT through CIFRE PhD program. We also thank the FEDER program through the SaphirTEC project. The authors thank Amplitude company for their support and Scientific Visual company for their exchange on no destructive sapphire large scale crystal characterization.

References

1 V. Pishchik, L. A. Lytvynov and E. R. Dobrovinskaya, *Sapphire: Material, Manufacturing, Applications*, Springer US, Boston, MA, 2009, DOI: 10.1007/978-0-387-85695-7.
2 P. F. Moulton, Spectroscopic and laser characteristics of Ti:Al_2O_3, *J. Opt. Soc. Am. B*, 1986, **3**(1), 125, DOI: 10.1364/JOSAB.3.000125.
3 J. Dong and P. Z. Deng, Ti:sapphire crystal used in ultrafast lasers and amplifiers, *J. Cryst. Growth*, 2004, **261**(4), 514–519, DOI: 10.1016/j.jcrysgro.2003.09.049.
4 V. A. Tatartchenko, Sapphire Crystal Growth and Applications, in *Wiley Series in Materials for Electronic and Optoelectronic Applications*, John Wiley & Sons Ltd, Chichester, 2005, pp. 299–338.
5 L. Xuan and T. Duffar, The growth of titanium doped sapphire for laser application, *Prog. Cryst. Growth Charact. Mater.*, 2025, **71**(2), 100666, DOI: 10.1016/j.pcrysgrow.2025.100666.

6 G. Boulon, Fifty years of advances in solid-state laser materials, *Opt. Mater.*, 2012, **34**(3), 499–512, DOI: 10.1016/j.optmat.2011.04.018.
7 H. Fattahi, H. G. Barros, M. Gorjan, T. Nubbemeyer, B. Alsaif, C. Y. Teisset, M. Schultze, S. Prinz, M. Haefner, M. Ueffing, A. Alismail, L. Vamos, A. Schwarz, O. Pronin, J. Brons, X. T. Geng, G. Arisholm, M. Ciappina, V. S. Yakovlev, D.-E. Kim, A. M. Azzeer, N. Karpowicz, D. Sutter, Z. Major, T. Metzger and F. Krausz, Third-generation femtosecond technology, *Optica*, 2014, **1**(1), 45–63, DOI: 10.1364/OPTICA.1.000045.
8 I. T. McKinnie, A. L. Oien, D. M. Warrington, P. N. Tonga, L. a. W. Gloster and T. A. King, Ti3+ ion concentration and Ti:sapphire laser performance, *IEEE J. Quantum Electron.*, 1997, **33**(7), 1221–1230, DOI: 10.1109/3.594888.
9 A. Kachanov, A. Charvat and F. Stoeckel, Intracavity Laser Spectroscopy with Vibronic Solid-State Lasers .1. Spectrotemporal Transient-Behavior of a Ti-Sapphire Laser, *J. Opt. Soc. Am. B*, 1994, **11**(12), 2412–2421, DOI: 10.1364/JOSAB.11.002412.
10 D. E. Spence, P. N. Kean and W. Sibbett, 60-fsec pulse generation from a self-mode-locked Ti:sapphire laser, *Opt. Lett.*, 1991, **16**(1), 42–44, DOI: 10.1364/OL.16.000042.
11 K. F. Wall, R. L. Aggarwal, P. A. Schulz, P. Lacovara, V. Daneu, A. Walther and A. Sanchez, A Ti:Al2O3 Master-Oscillator Power-Amplifier System, in *Advanced Solid State Lasers (1990)*, Optica Publishing Group, 1990, p. TLM7, DOI: 10.1364/ASSL.1990.TLM7.
12 G. A. Rines, P. F. Moulton and J. Harrison, Narrowband, High-Energy Ti:Al2O3 Lidar Transmitter for Spacecraft Sensing, in *Advanced Solid State Lasers (1989), paper AA1*, Optica Publishing Group, 1989, p. AA1, DOI: 10.1364/ASSL.1989.AA1.
13 H. K. Soong and J. B. Malta, Femtosecond Lasers in Ophthalmology, *Am. J. Ophthalmol.*, 2009, **147**(2), 189–197, DOI: 10.1016/j.ajo.2008.08.026.
14 K. F. Wall and A. Sanchez, Titanium sapphire lasers, *Lincoln Laboratory Journal*, 1990, **3**(3), 447–469.
15 P. W. Roth, D. Burns and A. J. Kemp, Power scaling of a directly diode-laser-pumped Ti:sapphire laser, *Opt. Express*, 2012, **20**(18), 20629–20634, DOI: 10.1364/OE.20.020629.
16 K. Gürel, V. J. Wittwer, M. Hoffmann, C. J. Saraceno, S. Hakobyan, B. Resan, A. Rohrbacher, K. Weingarten, S. Schilt and T. Südmeyer, Green-diode-pumped femtosecond Ti:Sapphire laser with up to 450 mW average power, *Opt. Express*, 2015, **23**(23), 30043–30048, DOI: 10.1364/OE.23.030043.
17 M. Klejch, M. Němec, J. Kubát and J. Polák, Preparation, properties and application of sapphire single-crystal fibers grown by the EFG method, *EPJ Web Conf.*, 2013, **48**, 00007, DOI: 10.1051/epjconf/20134800007.
18 F. J. Bruni, C.-M. Liu and J. Stone-Sundberg, Will Czochralski Growth of Sapphire Once Again Prevail?, *Acta Phys. Pol. A*, 2013, **124**(2), 213–218, DOI: 10.12693/APhysPolA.124.213.
19 S. V. Vyshnevskiy, Y. V. Kryvonosov, L. A. Lytvynov and S. D. Vyshnevskiy, Foreign phase inclusions in Ti-sapphire grown in a carbon containing medium.pdf, *Funct. Mater.*, 2006, **13**(2), 238–244.
20 L. Zhang, H. Zuo, J. Zhou, J. Sun, D. Xing and J. Han, Haze in sapphire crystals grown by SAPMAC method, *Cryst. Res. Technol.*, 2011, **46**(7), 669–675, DOI: 10.1002/crat.201100122.
21 O. M. Bunoiu, T. Duffar and I. Nicoara, Gas bubbles in shaped sapphire, *Prog. Cryst. Growth Charact. Mater.*, 2010, **56**(3–4), 123–145, DOI: 10.1016/j.pcrysgrow.2010.09.001.
22 A. Vorob'ev, V. Kalaev and K. Mazaev, Chemical model of sapphire crystal growth by Ky technique, *J. Cryst. Growth*, 2023, **612**, 127196, DOI: 10.1016/j.jcrysgro.2023.127196.
23 W. Gui-gen, Z. Ming-fu, Z. Hong-bo, H. Xiao-dong and H. Jie-cai, Study on Inclusions in Large Sapphire Optical Crystal Grown by SAPMAC Method, *Chin. J. Aeronaut.*, 2006, 31–35.
24 H. Li, E. A. Ghezal, G. Alombert-Goget, G. Breton, J. M. Ingargiola, A. Brenier and K. Lebbou, Qualitative and quantitative bubbles defects analysis in undoped and Ti-doped sapphire crystals grown by Czochralski technique, *Opt. Mater.*, 2014, **37**, 132–138, DOI: 10.1016/j.optmat.2014.05.012.
25 E. A. Ghezal, H. Li, A. Nehari, G. Alombert-Goget, A. Brenier, K. Lebbou, M. F. Joubertt and M. T. Soltani, X Effect of Pulling Rate on Bubbles Distribution in Sapphire Crystals Grown by the Micropulling Down (μ-PD) Technique, *Cryst. Growth Des.*, 2012, **12**(8), 4098–4103, DOI: 10.1021/cg300589h.
26 L. Wollesen, A. Nehari, S. Labor, G. Alombert-Goget, D. Guignier and K. Lebbou, Bubble distribution in shaped sapphire grown from molybdenum crucibles using the micro-pulling down technique, *CrystEngComm*, 2025, **27**(4), 497–506, DOI: 10.1039/D4CE01077A.
27 R. Bouaita, G. Alombert-Goget, E. A. Ghezal, A. Nehari, O. Benamara, M. Benchiheub, G. Cagnoli, K. Yamamoto, X. Xu, V. Motto-Ros, H. Li, C. Dujardin and K. Lebbou, Seed orientation and pulling rate effects on bubbles and strain distribution on a sapphire crystal grown by the micro-pulling down method, *CrystEngComm*, 2019, **21**(28), 4200–4211, DOI: 10.1039/C9CE00510B.
28 E. A. Ghezal, A. Nehari, K. Lebbou and T. Duffar, Observation of Gas Bubble Incorporation during Micropulling-Down Growth of Sapphire, *Cryst. Growth Des.*, 2012, **12**(11), 5715–5719, DOI: 10.1021/cg301232r.
29 A. Nehari, T. Duffar, E. A. Ghezal and K. Lebbou, Chemical Segregation of Titanium in Sapphire Single Crystals Grown by Micro-Pulling-Down Technique: Analytical Model and Experiments, *Cryst. Growth Des.*, 2014, **14**(12), 6492–6496, DOI: 10.1021/cg5013582.
30 H. Li, Bubbles propagation in undoped and Titanium, *PhD thesis*, UCBL, France, 2014.
31 H. Li, E. A. Ghezal, A. Nehari, G. Alombert-Goget, A. Brenier and K. Lebbou, X Bubbles defects distribution in sapphire bulk crystals grown by Czochralski technique, *Opt. Mater.*, 2013, **35**(5), 1071–1076, DOI: 10.1016/j.optmat.2012.12.022.
32 A. Nehari, A. Brenier, G. Panzer, K. Lebbou, J. Godfroy, S. Labor, H. Legal, G. Chériaux, J. P. Chambaret, T. Duffar and

R. Moncorgé, Ti-Doped Sapphire (Al_2O_3) Single Crystals Grown by the Kyropoulos Technique and Optical Characterizations, *Cryst. Growth Des.*, 2011, **11**(2), 445–448, DOI: 10.1021/cg101190q.

33 G. Alombert-Goget, K. Lebbou, N. Barthalay, H. Legal and G. Chériaux, Large Ti-doped sapphire bulk crystal for high power laser applications, *Opt. Mater.*, 2014, **36**(12), 2004–2006, DOI: 10.1016/j.optmat.2014.01.011.

34 G. Alombert-Goget, G. Sen, C. Pezzani, N. Barthalay, T. Duffar and K. Lebbou, Large Ti-doped sapphire single crystals grown by the kyropoulos technique for petawatt power laser application, *Opt. Mater.*, 2016, **61**, 21–24, DOI: 10.1016/j.optmat.2016.04.025.

35 G. Alombert-Goget, Y. Guyot, A. Nehari, O. Benamara, N. Blanchard, A. Brenier, N. Barthalay and K. Lebbou, Scattering defect in large diameter titanium-doped sapphire crystals grown by the Kyropoulos technique, *CrystEngComm*, 2018, **20**(4), 412–419, DOI: 10.1039/C7CE02004J.

36 H. S. Fang, Q. J. Zhang, J. Tian, S. Wang and R. H. Ma, Study of internal radiation with solute inclusions during Czochralski sapphire crystal growth, *Int. J. Heat Mass Transfer*, 2014, **79**, 783–789, DOI: 10.1016/j.ijheatmasstransfer.2014.08.093.

37 H. S. Fang, Y. Y. Pan, L. L. Zheng, Q. J. Zhang, S. Wang and Z. L. Jin, To investigate interface shape and thermal stress during sapphire single crystal growth by the Cz method, *J. Cryst. Growth*, 2013, **363**, 25–32, DOI: 10.1016/j.jcrysgro.2012.09.050.

38 I. Lasloudji, F. Mokhtari, A. Nehari, G. Alombert-Goget and K. Lebbou, Experimental and numerical effects of active afterheater addition on the growth of langatate ($La_3Ga_{5.5}Ta_{0.5}O_{14}$) crystals by the Czochralski method, *CrystEngComm*, 2018, **20**(8), 1110–1115, DOI: 10.1039/c7ce02032e.

39 L. Xuan and T. Duffar, Physico-chemical model for dopant charge state conversion during Ti:sapphire crystal growth, *J. Cryst. Growth*, 2021, **570**, 126234, DOI: 10.1016/j.jcrysgro.2021.126234.

40 Y. Z. Bouzouaoui, F. Mokhtari, M. Velázquez, S. Zermout and I. Lasloudji, Effect of the growth pulling direction on 3D anisotropic stress during different stages of semitransparent Li2MoO4 growth, *CrystEngComm*, 2021, **23**(48), 8612–8621, DOI: 10.1039/D1CE00766A.

41 F. Haddad, Y. Z. Bouzouaoui, F. Mokhtari, M. Velazquez, S. Zermout and I. Lasloudji, Computational Analysis of Radiative Heat Transfer in Czochralski Furnace and 3D Anisotropic Thermal Stress in Li2MoO4 Bulk Crystal, *Cryst. Res. Technol.*, 2022, **57**(10), 2200097, DOI: 10.1002/crat.202200097.

42 S. E. Demina, E. N. Bystrova, M. A. Lukanina, V. M. Mamedov, V. S. Yuferev, E. V. Eskov, M. V. Nikolenko, V. S. Postolov and V. V. Kalaev, Numerical analysis of sapphire crystal growth by the Kyropoulos technique, *Opt. Mater.*, 2007, **30**(1), 62–65, DOI: 10.1016/j.optmat.2006.11.012.

43 S. E. Demina, E. N. Bystrova, V. S. Postolov, E. V. Eskov, M. V. Nikolenko, D. A. Marshanin, V. S. Yuferev and V. V. Kalaev, Use of numerical simulation for growing high-quality sapphire crystals by the Kyropoulos method, *J. Cryst. Growth*, 2008, **310**(7–9), 1443–1447, DOI: 10.1016/j.jcrysgro.2007.11.083.

44 Z. L. Jin, H. S. Fang, N. Yang, Z. Zhang, S. Wang and J. F. Xu, Influence of temperature-dependent thermophysical properties of sapphire on the modeling of Kyropoulos cooling process, *J. Cryst. Growth*, 2014, **405**, 52–58, DOI: 10.1016/j.jcrysgro.2014.07.049.

45 C.-H. Chen, J.-C. Chen, C.-W. Lu and C.-M. Liu, Numerical simulation of heat and fluid flows for sapphire single crystal growth by the Kyropoulos method, *J. Cryst. Growth*, 2011, **318**(1), 162–167, DOI: 10.1016/j.jcrysgro.2010.10.121.

46 S. Zermout, F. Mokhtari, A. Nehari and I. Lasloudji, Numerical study on the effect of additional resistive heating and crystal rotation on sapphire single crystals (Al_2O_3) grown by the Kyropoulos method, *CrystEngComm*, 2018, **20**(35), 5220–5227, DOI: 10.1039/C8CE00972D.

47 S. Zermout, F. Mokhtari, A. Nehari, I. Lasloudji, F. Haddad and A. Merah, 3D Anisotropic Stress Analysis during Kyropoulos Growth of Sapphire Single Crystal, *Cryst. Res. Technol.*, 2019, **54**(8), 1900058, DOI: 10.1002/crat.201900058.

48 C. W. Lan, S. Uda and T. Fukuda, Theoretical analysis of the micro-pulling-down process for GexSi1-x fiber crystal growth, *J. Cryst. Growth*, 1998, **193**(4), 552–562, DOI: 10.1016/S0022-0248(98)00527-2.

49 G. Samanta, A. Yeckel, P. Daggolu, H. Fang, E. D. Bourret-Courchesne and J. J. Derby, Analysis of limits for sapphire growth in a micro-pulling-down system, *J. Cryst. Growth*, 2011, **335**(1), 148–159, DOI: 10.1016/j.jcrysgro.2011.09.015.

50 G. Samanta, A. Yeckel, E. D. Bourret-Courchesne and J. J. Derby, Parametric sensitivity and temporal dynamics of sapphire crystal growth via the micro-pulling-down method, *J. Cryst. Growth*, 2012, **359**, 99–106, DOI: 10.1016/j.jcrysgro.2012.08.037.

51 H. S. Fang, Z. W. Yan and E. D. Bourret-Courchesne, Numerical Study of the Micro-Pulling-Down Process for Sapphire Fiber Crystal Growth, *Cryst. Growth Des.*, 2011, **11**(1), 121–129, DOI: 10.1021/cg101021t.

52 Z. Zeng, L. Qiao, Y. Liu, Y. Yokota, Y. Kawazoe and A. Yoshikawa, Numerical study on the radial dopant distribution in micro-pulling-down crystal growth, *J. Cryst. Growth*, 2016, **434**, 110–115, DOI: 10.1016/j.jcrysgro.2015.10.029.

53 W. Su, T. Duffar, A. Nehari, V. Kononets and K. Lebbou, Modeling of dopant segregation in sapphire single crystal fibre growth by Micro-Pulling-Down method, *J. Cryst. Growth*, 2017, **474**, 43–49, DOI: 10.1016/j.jcrysgro.2016.12.075.

54 R. Murakami, K. Oikawa, K. Kamada, S. Itoi and A. Yoshikawa, Effects of crystal growth rate and pressure on shape controllability in the dewetting micro-pulling-down method, *J. Cryst. Growth*, 2024, **629**, 127565, DOI: 10.1016/j.jcrysgro.2023.127565.

55 F. Mokhtari, L. Wollesen, A. Nehari and K. Lebbou, Experimental and Numerical Analysis on Bubble Behavior in

sapphire Rods grown by Micro-Pulling-Down, *Mater. Res. Bull.*, 2025, **197**, 113933, DOI: 10.1016/j.materresbull.2025.113933.

56 L. Wollesen, A. Nehari, S. Labor, G. Alombert-Goget, D. Guignier and K. Lebbou, Impact of graphite and alumina ceramic thermal insulation on the growth of undoped sapphire plates by micro-pulling down, *Mater. Res. Bull.*, 2026, **195**, 113846, DOI: 10.1016/j.materresbull.2025.113846.

57 P. Rudolph, K. Yoshikawa and T. Fukuda, Studies on meniscus and diameter stability during the growth of fiber crystals by the micro-pulling-down method, *Jpn. J. Appl. Phys., Part 1*, 2000, **39**(10), 5966–5969, DOI: 10.1143/JJAP.39.5966.

58 G.-Y. Ren, X.-H. Qu and S. Ding, A Real-Time Measurement Method of Air Refractive Index Based on Special Material Etalon, *Appl. Sci.*, 2018, **8**(11), 2325, DOI: 10.3390/app8112325.

59 X. Yang, T. Qiao, H. Zhang, H. Chen and G. Hao, Research on image recognition and detection method of sapphire bubbles, *J. Instrum.*, 2019, **14**(12), P12013, DOI: 10.1088/1748-0221/14/12/P12013.

60 Z. Meng, X. Zhai, J. Wei, Z. Wang and H. Wu, Absolute Measurement of the Refractive Index of Water by a Mode-Locked Laser at 518 nm, *Sensors*, 2018, **18**(4), 1143, DOI: 10.3390/s18041143.

61 Z. Rappoport, *CRC Handbook Of Tables For Organic Compound Identification*, 3rd edn, 1967, http://archive.org/details/crc-handbook-of-tables-for-organic-compound-identification-3rd-ed.

62 G. G. Stokes, On the Effect of the Internal Friction of Fluids on the Motion of Pendulums, in *Mathematical and Physical Papers*, Cambridge Library Collection - Mathematics, Cambridge Univ. Press, Cambridge, U.K., 1850, vol. 3, pp. 1–10, DOI: 10.1017/CBO9780511702266.002.

63 G. K. Batchelor, *An Introduction to fluid dynamics*, 14. print. in Cambridge mathematical library, Cambridge Univ. Press, Cambridge, 2010.

64 R. Clift, J. R. Grace and M. E. Weber, *Bubbles, Drops, and Particles*, Courier Corporation, 1978.

65 M. Cable and J. Frade, The Effects of Viscosity on the Behavior of Bubbles in Viscous-Liquids, *Phys. Chem. Glasses*, 1994, **35**(6), 231–238.

